Journal of Power Sources 196 (2011) 3887–3893

Contents lists available at ScienceDirect

Journal of Power Sources

journal homepage: www.elsevier.com/locate/jpowsour

Facile synthesis of hierarchically structured Fe_3O_4/carbon micro-flowers and their application to lithium-ion battery anodes

Shuangling Jin, Honggui Deng, Donghui Long*, Xiaojun Liu, Liang Zhan, Xiaoyi Liang, Wenming Qiao, Licheng Ling*

State Key Laboratory of Chemical Engineering, East China University of Science and Technology, 130 Meilong Road, Shanghai 200237, PR China

ARTICLE INFO

Article history:
Received 14 September 2010
Received in revised form
21 November 2010
Accepted 20 December 2010
Available online 7 January 2011

Keywords:
Lithium-ion battery
Anode
Nanocomposite
Magnetite
Carbon

ABSTRACT

A flower-like Fe_3O_4/carbon nanocomposite with nano/micro hierarchical structure is prepared by controlled thermal decomposition of the iron alkoxide precursor, which is obtained via an ethylene glycol-mediated solvothermal reaction of $FeCl_3$ and hexamethylenetetramine (HMT) in the absence of any surfactant. The nanocomposite is characterized by the assembly of porous nanoflakes consisting of Fe_3O_4 nanoparticles and amorphous carbon that is in situ generated from the organic components of alkoxide precursor. When used as the anode materials for the lithium-ion batteries, the resultant nanocomposite shows high capacity and good cycle stability (1030 m Ah g^{-1} at a current density of 0.2 C up to 150 cycles), as well as enhanced rate capability. The excellent electrochemical performance can be attributed to the high structural stability and high rate of ionic/electronic conduction arising from the synergetic effect of the unique nano/micro hierarchical structure and conductive carbon coating.

1. Introduction

Since the early 1990s, rechargeable lithium-ion batteries have been widely used as power sources for various portable electronic devices such as cellular phones, digital cameras, laptop computers and MP3 players [1]. For new generations of rechargeable lithium batteries, they applied not only to modern consumer electronics but also especially to hybrid electric vehicles and clean energy storage. The challenges are, naturally, to achieve higher specific energy density, higher specific power density, longer cycle life and lower cost. These demands create strong motivations behind the research and development of novel electrode materials with improved electrochemical performance for lithium-ion batteries. Transition metal oxides represent a new type of anode materials for lithium-ion batteries [2]. These metal oxides with interstitial-free structure can react with Li via the conversion reaction of $MO_x + 2xLi = M + xLi_2O$, which has been shown to exhibit lager rechargeable capacity, making them promising anode materials for new generations of lithium-ion batteries.

Among transition metal oxides, Magnetite (Fe_3O_4) is one of most attractive materials on economic and environmental grounds. However, its application in practical batteries is hindered due to its poor cycling stability resulting from large volume expansion occurring during cycling and low rate performance arising from kinetic limitations [3]. Extensive work to solve these problems has majorly focused on fabricating Fe_3O_4/carbon nanocomposites, which include (i) the composites with Fe_3O_4 nanoparticles embedded in a disordered carbon matrix [4–6], and (ii) single-particle-coating Fe_3O_4/carbon nanocomposites [7–9]. However, it is hard to homogeneously disperse the high-surface-energy nanoparticles in a carbon matrix during preparation process. As a result, the active nanoparticles severely agglomerate to form irregularly shaped secondary aggregates, which are detrimental to the stability of composite electrodes. Similarly, the interfacial energy of nanoparticles after carbon coating is still large and the composite particles tend to aggregate easily. And the carbon coating cannot effectively release the large strain caused by volume expansion because it tightly wraps the surface of the active particles. Therefore, the improvement in cyclability and/or rate performance of Fe_3O_4 is still limited. To further enhance the performance of Fe_3O_4 as anode materials in lithium-ion batteries, Fe_3O_4/carbon composite with rationally designed nanostructure is necessary.

In this study, a new kind of Fe_3O_4/carbon nanocomposite with flower-like nano/micro hierarchical structure is prepared by controlled thermal decomposition of the iron alkoxide precursor in inert atmosphere. The nanocomposite is characterized by the assembly of porous nanoflakes consisting of Fe_3O_4 nanoparticles and amorphous carbon that is in situ generated from the organic components of alkoxide precursor. This specific

* Corresponding authors. Tel.: +86 21 64252934; fax: +86 21 64252914.
E-mail addresses: longdh@mail.ecust.edu.cn (D. Long), lchling@ecust.edu.cn (L. Ling).

0378-7753/$ – see front matter © 2011 Elsevier B.V. All rights reserved.
doi:10.1016/j.jpowsour.2010.12.078

configuration results in micrometer-sized particles, which guarantees stability and manageability of the material, while still taking advantage of the nanoscale active materials in achieving the high capacity and the interspaces between nanoflakes in releasing the volume expansion. The carbon coating serves simultaneously as a physical barrier to prevent the aggregation of Fe_3O_4 nanoparticles during cycling and a conductive network to improve the local conductivity, which helps to realize the full potential of Fe_3O_4/carbon composite. Therefore, when employed as anodes for lithium-ion batteries, the as-obtained nanocomposite exhibits exceptional capacity retention and good rate capability.

2. Experimental

2.1. Materials preparation

In a typical synthesis, 0.4 g of $FeCl_3{\cdot}6H_2O$ and 1.0 g of HMT were added to 60 mL of ethylene glycol under magnetic stirring to give a cloudy solution. The resultant mixture was transferred to a 90 mL Teflon-lined autoclave, then sealed and heated at 160 °C for 6 h. After the reaction was cooled to room temperature, a green alkoxide precursor was obtained. The product was harvested by centrifugation and washed with alcohol several times before drying at 60 °C in an oven overnight. Afterwards the green powder was heated to 450 or 600 °C at a rate of 5 °C min^{-1} and maintained at this temperature for 3 h under the nitrogen flow to obtain the black powder. Meanwhile, some alkoxide precursors were calcined in air at 450 °C for 3 h with a temperature ramp of 1 °C min^{-1} to obtain the red powder. The samples prepared under nitrogen at 450 °C and 600 °C and in air at 450 °C were designated as N450, N600 and A450, respectively.

2.2. Materials characterization

The phase and composition of the products were characterized by X-ray powder diffraction (XRD, Rigaku D/max-2500 diffractometer with Cu Kα radiation, λ = 0.1542 nm, 40 kV, 100 mA), Raman spectra (Renishaw inVia + Reflex Raman spectrometer, excitation wavelength 514 nm), and inductively coupled plasma-optical emission spectroscopy (ICP, Thermo Elemental IRIS 1000). The morphology and structure of the products were observed under scanning electron microscopy (SEM, FEI Quanta 200F) and transmission electron microscopy (TEM, JEOL 2100F). Thermogravimetric/differential scanning calorimetry (TG/DSC) was performed on SDT Q600 thermal analyzer under nitrogen or air with a heating rate of 10 °C min^{-1} from ambient temperature to 1000 °C. The specific surface area was measured by the Brunauer–Emmett–Teller (BET) method using nitrogen adsorption–desorption isotherms on a Micrometrics ASAP 2020 system, and the pore size distribution was obtained from the desorption branch of the isotherm by the Barrett–Joyner–Halenda (BJH) method.

2.3. Electrochemical measurements

To evaluate the electrochemical performance, coin-type half cells were assembled using the as-prepared product as anode material for lithium-ion battery. The working electrodes were prepared by dispersing in N-methyl-2-pyrrolidone (NMP) a blend of as-obtained active material, acetylene black, and polyvinylidene difluoride (PVDF) at the weight percent ratio of 75:15:10. The slurry was then pasted onto a copper foil and dried in vacuum at 120 °C overnight. The model cells were fabricated using lithium foil as the counter electrode and the reference electrode, Celgard 2400 as the separator, and a solution of 1 M $LiPF_6$ in ethylene carbonate (EC)/dimethyl carbonate (DMC)/diethyl carbonate (DEC) (1:1:1, in wt%) as the electrolyte. The assembly was carried out in an argon-filled glove box with oxygen and moisture levels less than 1 ppm. The discharge–charge tests were performed in the voltage range of 0.01–3.0 V (vs. Li/Li^+) at current rates from 0.2 C to 5 C (1 C = 924 mA g^{-1} for sample N450 and N600, and 1 C = 1007 mA g^{-1} for sample A450). Cyclic voltammograms (CV) were recorded between 3.0 and 0.0 V at a scan rate of 0.1 mV s^{-1}. All the electrochemical tests were performed at room temperature. Note that both the current density and specific capacity were calculated on the base of mass of the composite rather than that of Fe_3O_4, unless otherwise stated.

3. Results and discussion

3.1. Structure and morphology of the alkoxide precursor

Fig. 1a and b shows the typical SEM and TEM images of the precursor, which is composed of 3D flowerlike architectures with a diameter approximately 2 μm. The entire architecture is built from several dozens petal-like nanoflakes with smooth surfaces. These nanoflakes are about 50 nm thick and 1 μm wide, and connect with each other through the center to form 3D flowerlike structure. The XRD diffraction peaks of the precursor (Fig. 1c) are very similar to those of the reported metal alkoxides [10–14], especially the strong peak located in the low-angle region (around 11°). Thus, the as-synthesized precursor should be one kind of iron alkoxide.

When ethylene glycol molecules lose protons and coordinate with $FeCl_3$ to form iron alkoxide, HCl is generated as reported in the reaction between ethylene glycol and metal chloride [10,15]. If HCl cannot be removed, the accumulation of HCl will inhibit further iron alkoxide formation. In this work, HMT is employed as an accelerant, which can be decomposed into formaldehyde and ammonia [16]. The ammonia can further hydrolyze to OH^- and then neutralize the HCl, promoting the formation of iron alkoxide.

3.2. Structure, composition, and morphology of the heat-treated products

Thermal decomposition behaviors of the alkoxide precursor under air and nitrogen were monitored by TG and DSC, as shown in Fig. 2. When the precursor is heated in air, the DSC curve exhibits an intensive exothermic peak around 279 °C, corresponding with the weight loss from 230 to 300 °C in TG curve, which can be attributed to the combustion of organic species and the formation of Fe_2O_3. By contrast, two noticeable weight loss stages can be observed in the TG curve of the precursor under nitrogen flow. The first weight loss stage begins from 270 °C to 400 °C with two exothermic peaks at 257 °C and 320 °C, which could be ascribed to the formation of Fe_3O_4 and carbon through decomposition of the precursor. The second weight loss stage is detected from 600 to 700 °C, with an endothermic peak around 672 °C in DSC curve, indicating the reduction of Fe_3O_4 by carbon species.

XRD patterns of the products after thermal decomposition under different conditions are given in Fig. 3. When the precursor is annealed at 450 °C under nitrogen, the diffraction peaks of the product N450 match well with those of the Fe_3O_4 (Magnetite, JCPDS No. 74-1910). The γ-Fe_2O_3 phase has similar XRD patterns to Fe_3O_4, but it cannot exist at the heat-treatment temperature as it converts to α-Fe_2O_3 at about 400 °C [7]. No diffraction peaks corresponding to α-Fe_2O_3 found in the XRD pattern suggests the absence of γ-Fe_2O_3 phase. Furthermore, although the diffraction patterns look similar for Fe_3O_4 and γ-Fe_2O_3, they are different with different space groups (Fd3m and $P4_232$ for Fe_3O_4 and γ-Fe_2O_3, respectively) and lattice parameters that differ significantly (8.390 Å and 8.350 Å for Fe_3O_4 and γ-Fe_2O_3, respectively, JCPDS Nos. 74-1910 and 24-0081).

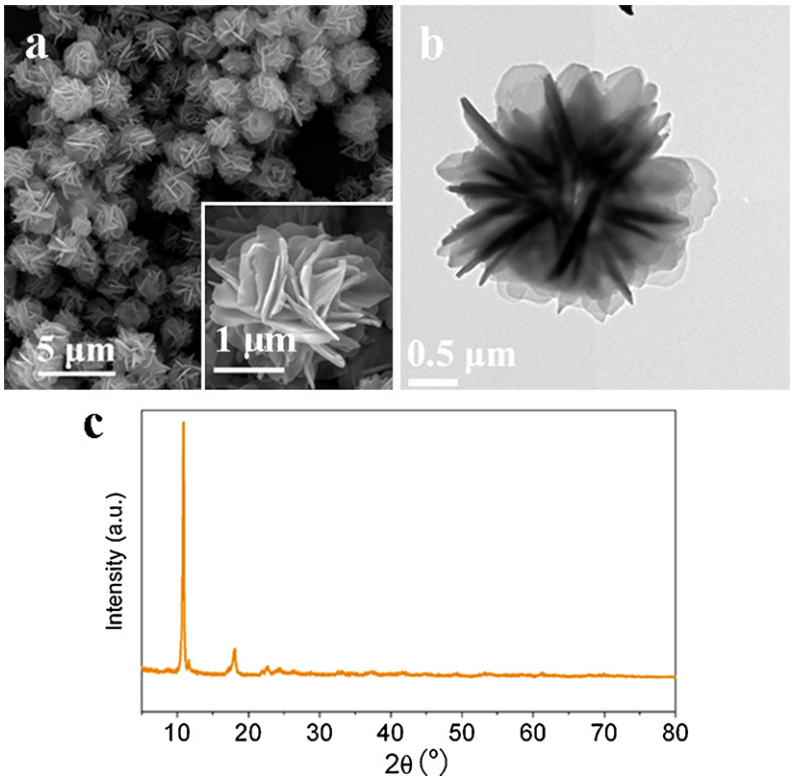

Fig. 1. (a) SEM and (b) TEM images, and (c) XRD pattern of the precursor. The inset in (a) is a SEM image of the individual flowerlike structure of the precursor.

Refinement carried out by using the MDI Jade 5.0 software yielded cubic lattice parameters of 8.386 (7) Å, in good agreement with literature values. Therefore, it can be concluded that the product N450 is Fe_3O_4 rather than γ-Fe_2O_3. The mean crystallite size of Fe_3O_4 in the sample N450 is calculated to be about 11.1 nm using the Scherrer's formula based on the peaks of (2 2 0) and (3 1 1). The graphitic structure of carbon species cannot be detected by XRD, possibly because their crystalline sizes are very fine and amorphous. As the annealing temperature under nitrogen up to 600 °C, ferrous oxide FeO (Wuestite, JCPDS 75-1550) and elemental iron Fe (iron, JCPDS 87-0721) besides Fe_3O_4 are also detected in the product N600, suggesting that Fe_3O_4 is partially reduced by the carbon. The approximate crystallite sizes in the composite were estimated to be 16.9 nm for the Fe_3O_4, 8.7 nm for the FeO and 38.4 nm for the Fe, respectively, using the Scherrer's equation, where (2 2 0) peak was used for Fe_3O_4, (2 0 0) peak for FeO, and (1 1 0) peak for Fe. When the iron alkoxide precursor is calcined at 450 °C in air, the diffraction peaks of the product A450 are in good agreement with those of α-Fe_2O_3 (Hematite, JCPDS 87-1166) with an average crystallite size of about 29.6 nm estimated from the width of (1 0 4) peak by Scherrer's formula.

Raman spectroscopy was further performed to analyze the phase composition of the products after thermal decomposition, as shown in Fig. 4. The spectrum of the iron alkoxide precursor contains many peaks, which are hard to be defined as the lack-

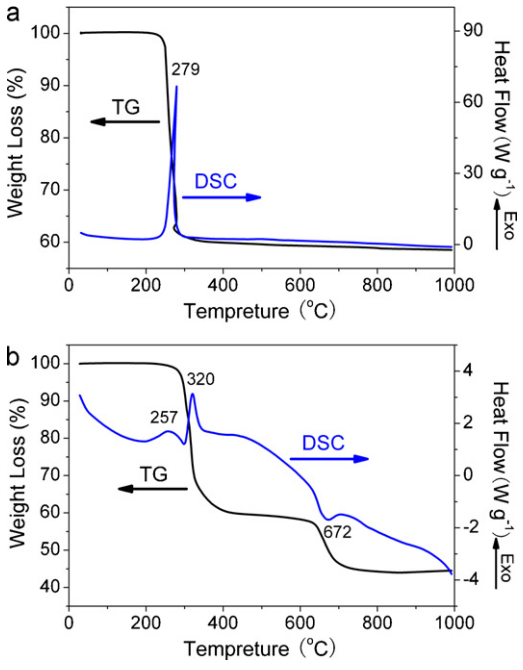

Fig. 2. TG/DSC curves of the precursor under (a) air and (b) nitrogen.

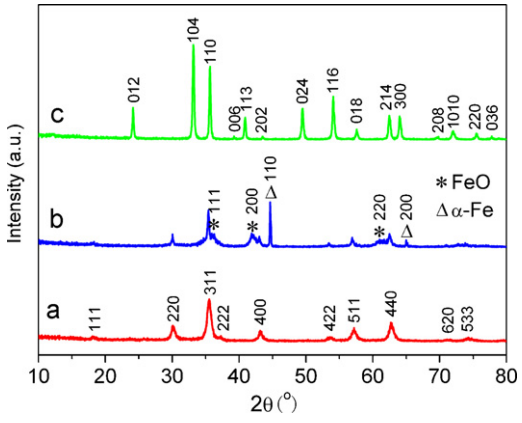

Fig. 3. XRD patterns of: (a) N450, (b) N600, and (c) A450.

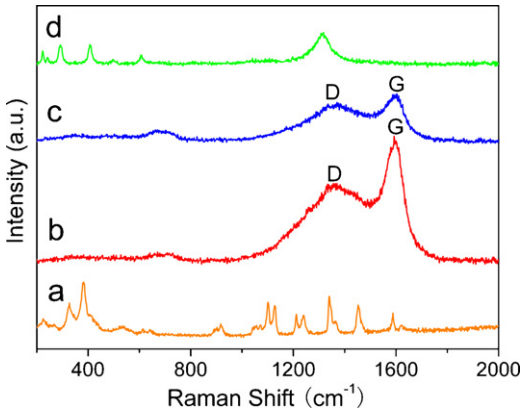

Fig. 4. Raman spectra of: (a) the precursor, (b) N450, (c) N600, and (d) A450.

ing of information data. The spectrum of sample N450 consist of a relatively small band at 670 cm^{-1} corresponding to the A_{1g} mode of Fe_3O_4 [17] and two strong bands at 1356 and 1594 cm^{-1} corresponding to the fundamental D and G bands for carbon, respectively, confirming that sample N450 is composed of the magnetite Fe_3O_4 phase and carbon. Furthermore, ICP was used to reveal the precise chemical composition of the sample N450. The results showed that N450 has a chemical composition of 87.8 wt% Fe_3O_4 and 12.2 wt% carbon. The Raman spectrum of sample N600 is similar with that of sample N450, indicating that this sample also contains some carbons. The spectrum of sample A450 exhibit several peaks, which can be assigned as the A_{1g} modes (222 and 498 cm^{-1}), E_g modes (242, 290, 408, and 605 cm^{-1}), and two-magnon scattering feature (1315 cm^{-1}) of the pure phase of α-Fe_2O_3 [18].

Fig. 5a and b displays the SEM images of sample N450, showing that heat treatment at 450 °C under nitrogen did not change the total flowerlike morphology of the precursor. Fig. 5c is a typical TEM image taken from the flake of an individual flowerlike structure shown in the inset. It can be seen that each piece of flake of the flowerlike structure has been transformed from a dense structure with a smooth surface into a highly porous structure consisting of well-dispersed nanoparticles. The size of these nanoparticles ranges from 10 to 20 nm, consistent with the XRD result estimated from Scherrer's formula. Fig. 5d shows the HRTEM image of the edge of the Fe_3O_4 nanoparticles, and a lattice spacing of 0.48 Å corresponding to (1 1 1) plane can be observed. The carbons could not be observed by TEM possibly due to their thin and disordered structure. Combined the Raman and ICP results, we think that the Fe_3O_4 nanoparticles are surrounded by a very thin conductive carbon layer which is in situ generated from the organic components of alkoxide precursor.

Calcination condition plays an important role in controlling the morphology and the texture of the products. As shown in Fig. 6a and b, when the calcination temperature under nitrogen increases to 600 °C, the flowerlike structure of the particles partially collapses, and the primary nanoparticles become markedly large and aggregate severely. These changes are attributed to the phase transformation during the reduction process, as demonstrated by the XRD results. The calcination of the precursor in air at 450 °C does not obviously change the flowerlike morphology but the nanoflakes consist of larger crystal nanoparticles (Fig. 6c and d). Therefore, the in situ generated carbon coating serves not only as a reducing agent to form a magnetite phase, but also as a physical barrier to suppress the growth of nanoparticles.

The nitrogen adsorption–desorption isotherms and corresponding BJH desorption pore size distributions of three samples are displayed in Fig. 7. All isotherms feature hysteresis between the

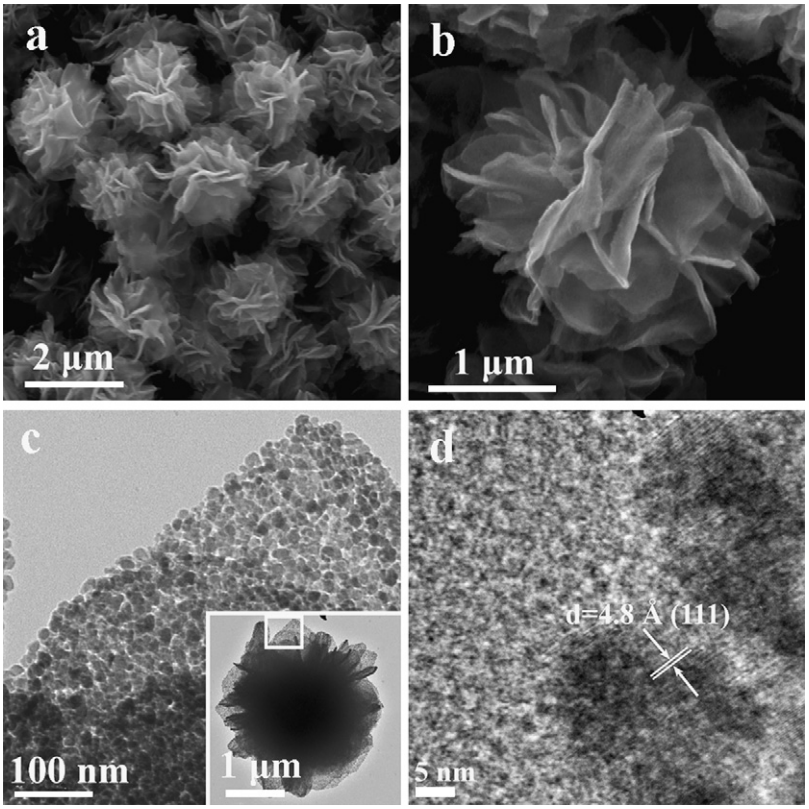

Fig. 5. (a) Low-magnification and (b) high-magnification SEM images of N450, (c) high-magnification TEM image of the flake of the flowerlike structure of N450 (inset) and (d) high-resolution TEM (HRTEM) image taken from the Fe_3O_4 nanoparticles.

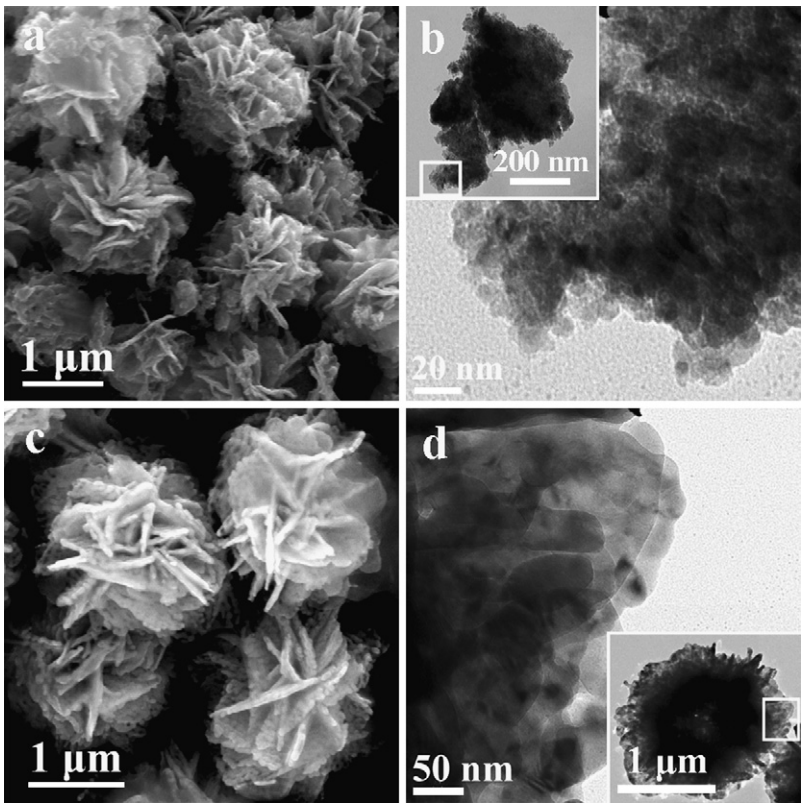

Fig. 6. (a) SEM image of N600, (b) high-magnification TEM image taken from the edge of an individual particle of N600 (inset), (c) SEM image of A450, and (d) high-magnification TEM image of the flake of the flowerlike structure of A450 (inset).

desorption and adsorption branches, indicating the presence of mesopores. The pore size distribution of sample N450 (inset of Fig. 7) is in the range 3–12 nm, and BET surface area is 61 $m^2 g^{-1}$. With a higher annealing temperature at 600 °C, an evident decrease in the surface area (21 $m^2 g^{-1}$) was observed, which could be ascribed to the large crystals of new phase and sintering within crystals. And for sample A450, the surface area is only 11 $m^2 g^{-1}$ due to the presence of large crystals, as verified by XRD and TEM results.

3.3. Electrochemical performance

Inspired by the unique structure of the as-obtained products under different conditions, we investigated their ability to reversibly insert/release lithium. Fig. 8 shows the CV curves of the samples N450, N600 and A450 for the first three cycles in the voltage range from 3.0 to 0.0 V at a scan rate of 0.1 mV s^{-1}. Three reduction peaks are observed in the first cathodic scan for sample N450. Two of them are around 1.5 V and 0.85 V, which are absent in the corresponding curve for sample N600 (Fig. 8b), might be ascribed to the formation of $Li_xFe_3O_4$ [4,19]. The difference between the CV curves of the two samples is possibly due to their different compositional and textural characteristics (partial reduction of Fe_3O_4 and particle sintering in sample N600) [20]. The third strong peak at around 0.5 V could be associated with the reduction of Fe^{3+} and Fe^{2+} to Fe^0 and the irreversible reaction related to the decomposition of the electrolyte [6]. The first anodic curves for samples N450 and N600 are similar and include a broad peak at about 1.7 V, corresponding to the reversible oxidation of Fe^0 to Fe^{3+}. In the second cycle, the peaks at 1.5 V and 0.85 V for sample N450 disappear, indicating that the reaction to form $Li_xFe_3O_4$ is irreversible. The CV curves of the two samples are stable and show good reversibility after the second cycle. In the case of sample A450 (Fig. 8c), the CV curves are similar to those reported for Fe_2O_3 [21,22]. The peak at 1.6 V in the first cathodic curve can be assigned to the formation of cubic $Li_xFe_2O_3$ and the strong peak at 0.6 V to the reduction from Fe^{2+} to Fe^0. The double peak observed on charging the cell can be attributed to a change in iron oxidation state in two steps (Fe^0 to Fe^{2+} at 1.7 V and Fe^{2+} to Fe^{3+} at 1.85 V).

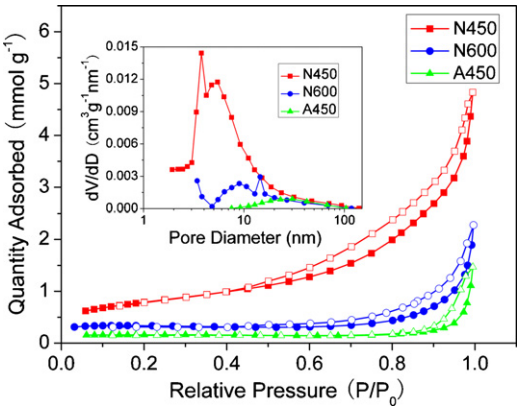

Fig. 7. Nitrogen adsorption–desorption isotherms at 77 K (filled symbols: adsorption and open symbols: desorption) with corresponding BJH desorption pore size distributions (inset) of N450, N600, and A450.

The charge/discharge curves of the three samples for the first five cycles obtained at a rate of 0.2 C in the voltage window of 0.01–3.0 V (vs. Li/Li^+) are shown in Fig. 9. The first specific discharge capacity of sample N450 is as high as 1502 m Ah g^{-1}, while that of N600 is 928 m Ah g^{-1}. From the fully discharged state, 69% (1038 m Ah g^{-1}, N450) and 70% (656 m Ah g^{-1}, N600) of the stored lithium can be extracted upon charging to 3 V. The initial discharge and charge capacities of sample A450 are 1354 and 1000 m Ah g^{-1},

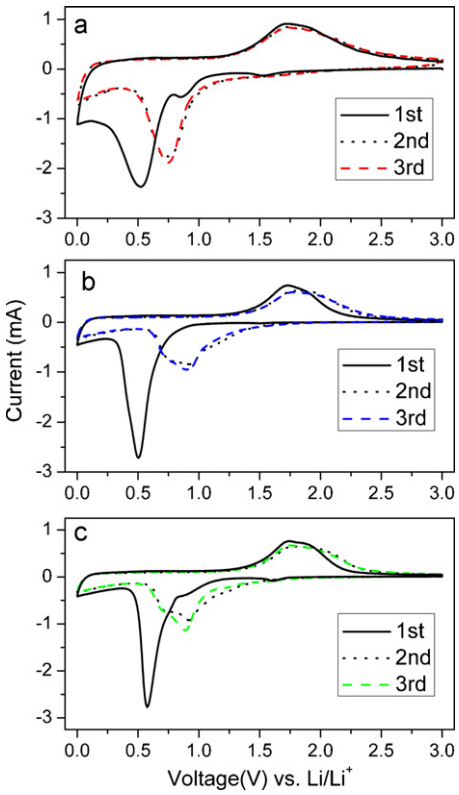

Fig. 8. Cyclic voltammograms of (a) N450, (b) N600, and (c) A450 from the first cycle to the third cycle at a scan rate of 0.1 mV s^{-1} in the voltage range of 0.0–3.0 V.

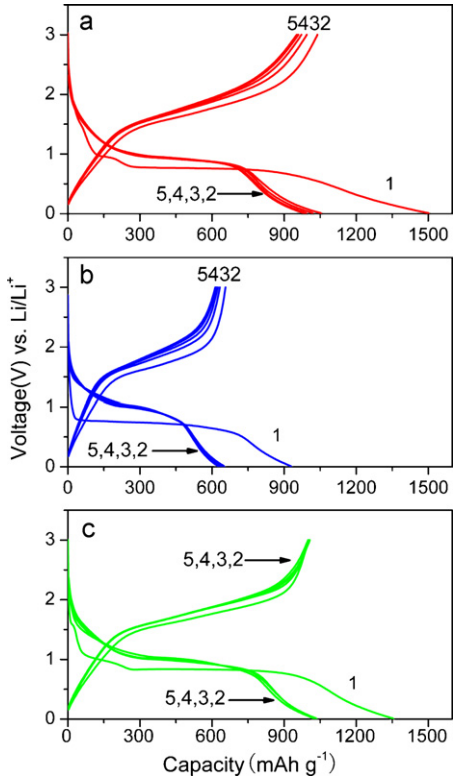

Fig. 9. The discharge/charge profiles of (a) N450, (b) N600, and (c) A450 in the voltage range 0.01–3.0 V at a current rate of 0.2 C.

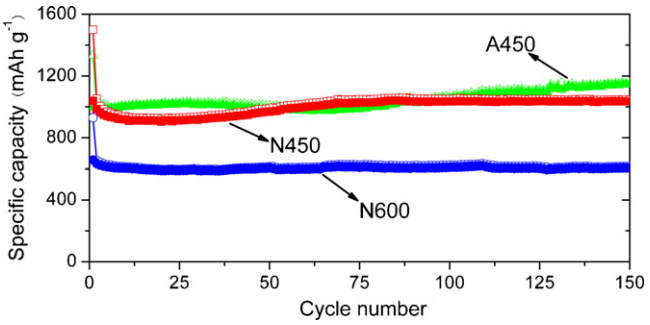

Fig. 10. Cycle performance of N450, N600, and A450 at a current rate of 0.2 C. Open symbols: discharge and filled symbols: charge.

respectively, showing a columbic efficiency of 74%. It is noted that the initial discharge capacities of N450 and N600 which are calculated on the basis of the whole mass exceed the theoretical capacity of Fe_3O_4 (924 m Ah g^{-1}), and that of A450 is also larger than the theoretical capacity of Fe_2O_3 (1007 m Ah g^{-1}). The phenomenon that the first discharge capacity considerably exceeds the theoretical capacity has been widely reported for transition metal oxides [22,23], which is usually ascribed to the formation of a polymeric gel-like film and possibly interfacial lithium storage. The coulombic efficiency of the first cycle for each sample is poor as a result of the high irreversible capacity observed during the first discharge process. This is typical behavior for systems containing nanostructured electrochemically active materials that create large electrode/electrolyte contact areas [24]. Nevertheless, after the first cycle, the coulombic efficiencies for the three samples are all above 95% in the subsequent cycles.

The three samples all have excellent cycling performance. Fig. 10 presents their long-cycle characteristics up to 150 cycles at a current rate of 0.2 C. For N450, the capacity drops to a minimum value of 921 m Ah g^{-1} over the first 20 cycles, then it increases gradually to 1030 m Ah g^{-1} until the 80th cycle, and finally it remains almost constant from the 80th to the 150th cycle. N600 delivers a capacity of about 610 m Ah g^{-1}, with excellent capacity retention up to 150 cycles. A450 retains a stable capacity of about 1000 m Ah g^{-1} in the first 80 cycles and increases gradually to 1150 m Ah g^{-1} at the 150th cycle. The capacity rise phenomenon has been widely referred in the transition metal oxide electrodes, which is attributed to the reversible growth of a polymeric gel-like film on the surface of the progressively pulverized particles resulting from electrochemical grinding effect [4,25–27]. The superior cycling performance of all samples comes from their unique hierarchical architecture. On the one hand, the interspaces between the nanoflakes guarantee the quick infiltration of electrolyte, and the nanometer-thick flakes with the porous structure consisting of nanoparticles afford short diffusion lengths for both Li-ion and electron transport. Thus, the kinetic performance of the electrode is better, the intercalation and extraction processes are of much higher efficiency, and therefore a higher effective specific capacity can be achieved. On the other hand, the interspaces between the nanoflakes can partially accommodate the volume expansion during Li insertion/extraction.

Note that the above cycling performance focused on a relatively low current rate (0.2 C). Considering the practical application, it is necessary to investigate the high rate performance of the as-prepared nanostructure d materials. The rate capabilities of the three samples from 0.2 C to 5 C for 10 cycles at each current rate are presented in Fig. 11. For sample N450, the initial charge capacity of 827, 691, 522, and 227 m Ah g^{-1} is observed as the current rate increases to 0.5, 1, 2, and 5 C, respectively. On the other hand, the initial charge capacity of sample N600 decreases to 532, 459, 380, and 199 m Ah g^{-1} at the same current rate as the sample

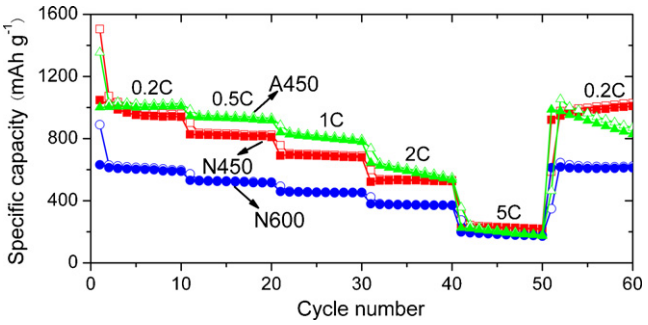

Fig. 11. Rate performance of N450, N600, and A450. Open symbols: discharge and closed symbols: charge.

N450. When the rate is lowered to 0.2 C, the capacity of 921 and 613 m Ah g^{-1} is regained for sample N450 and N600 respectively, demonstrating the reversibility of the two composites. When sample A450 cycles at high rates of 0.5, 1, 2, and 5 C, the initial charge capacity is 945, 840, 645, 225 m Ah g^{-1}, respectively. However, it cannot deliver a stable capacity during cycling at each high rate. The capacity decays slowly at the rate of 0.5 C, after which it declines rapidly at higher rates of 1, 2, and 5 C. When the current rate is again reduced back to 0.2 C, the capacity just shows a high initial value, then decreases markedly. These results clearly show that the carbon coating around the Fe_3O_4 nanoparticle plays an important role in improving the rate capability. The native carbon not only improves the local conductivity but also prevents the detachment and aggregation of possibly pulverized Fe_3O_4 nanoparticles during cycling. Without carbon, the pure α-Fe_2O_3 architectures cannot maintain the electrical continuity and structural integrity during cycling at high rates. Nevertheless, it should be noted that the cycling stability of these pure α-Fe_2O_3 architectures at low rates is significantly enhanced when compared to other α-Fe_2O_3 nanostructures because of their unique nano/micro hierarchical structures [23,28]. Furthermore, it is interesting to observe that the rate capability of sample N600 is better than N450, which should be attributed to the presence of metallic Fe. It has been reported that the electron transport to and within the particles is the main factor limiting the rate of iron oxide electrode [22]. For sample N600, the metallic Fe further enhances the electron transfer and reduces the resistance within the active nanoparticles, but the capacity of the composite is sacrificed due to the electrochemical inactivity of Fe.

4. Conclusions

In summary, we have developed a simple method for the large-scale synthesis of Fe_3O_4/carbon micro-flowers based on controlled calcination of the iron alkoxide precursor in inert atmosphere. The as-obtained Fe_3O_4/carbon nanocomposite exhibits high capacity, good cycle stability and enhanced rate capability as anode material in lithium-ion battery, due to its high structural stability and high rate of ionic/electronic conduction arising from the synergetic effect of the unique nano/micro hierarchical structure and conductive carbon coating. The utilization of carbon composite nano/micro hierarchical structure is suggested as a promising strategy toward the development of transition metal oxides as high-performance electrode materials for lithium-ion batteries. The method presented here could also be explored to fabricate other novel metal-oxide/carbon composite nanostructures via easy calcination of the organic/inorganic hybrid precursors for functional material applications.

Acknowledgements

This work was partly supported by National Science Foundation of China (Nos. 50730003 and 50672025), National Project of Scientific and Technical Supporting Programs Funded by Ministry of Science and Technology of China (No. 2007BAE55B00), National High Technology Research and Development Program of China (No. 2007AA05Z311), and Program for New Century Excellent Talents in University (NCET-07-0285).

References

[1] K. Ozawa, Solid State Ionics 69 (1994) 212–221.
[2] P. Poizot, S. Laruelle, S. Grugeon, L. Dupont, J.M. Tarascon, Nature 407 (2000) 496–499.
[3] S. Mitra, P. Poizot, A. Finke, J.M. Tarascon, Adv. Funct. Mater. 16 (2006) 2281–2287.
[4] L. Wang, Y. Yu, P.C. Chen, D.W. Zhang, C.H. Chen, J. Power Sources 183 (2008) 717–723.
[5] Z.M. Cui, L.Y. Jiang, W.G. Song, Y.G. Guo, Chem. Mater. 21 (2009) 1162–1166.
[6] Y.Z. Piao, H.S. Kim, Y.E. Sung, T. Hyeon, Chem. Commun. 46 (2010) 118–120.
[7] W.M. Zhang, X.L. Wu, J.S. Hu, Y.G. Guo, L.J. Wan, Adv. Funct. Mater. 18 (2008) 1–6.
[8] H. Liu, G.X. Wang, J.Z. Wang, D. Wexler, Electrochem. Commun. 10 (2008) 1879–1882.
[9] T. Muraliganth, A.V. Murugan, A. Manthiram, Chem. Commun. (2009) 7360–7362.
[10] L.S. Zhong, J.S. Hu, H.P. Liang, A.M. Cao, W.G. Song, L.J. Wan, Adv. Mater. 18 (2006) 2426–2431.
[11] S.W. Cao, Y.J. Zhu, M.Y. Ma, L. Li, L. Zhang, J. Phys. Chem. C 112 (2008) 1851–1856.
[12] S.W. Cao, Y.J. Zhu, J. Phys. Chem. C 112 (2008) 6253–6357.
[13] S.W. Cao, Y.J. Zhu, J. Phys. Chem. C 112 (2008) 12149–12156.
[14] D. Larcher, G. Sudant, R. Patrice, J.M. Tarascon, Chem. Mater. 15 (2003) 3543–3551.
[15] L.S. Zhong, J.S. Hu, H.P. Liang, A.M. Cao, Q. Liu, W.G. Song, L.J. Wan, Chem. Mater. 19 (2007) 1648–1655.
[16] B. Deng, A.W. Xu, G.Y. Chen, R.Q. Song, L.P. Chen, J. Phys. Chem. B 110 (2006) 11711–11716.
[17] D.L.A. de Faria, S. Venancio Silva, M.T. de Oliveira, J. Raman Spectrosc. 28 (1997) 873–878.
[18] S.H. Shim, T.S. Duffy, Am. Miner. 87 (2001) 318–326.
[19] Y. He, L. Huang, J.S. Cai, X.M. Zheng, S.G. Sun, Electrochim. Acta 55 (2010) 1140–1144.
[20] D. Larcher, C. Masquelier, D. Bonnin, Y. Chabre, V. Masson, J.B. Leriche, J.M. Tarascon, J. Electrochem. Soc. 150 (2003) A133–A139.
[21] J. Morales, L. Sanchez, F. Martin, F. Berry, X.L. Ren, J. Electrochem. Soc. 152 (2005) A1748–A1754.
[22] S.L. Chou, J.Z. Wang, D. Wexler, K. Konstantinov, C. Zhong, H.K. Liu, S.X. Dou, J. Mater. Chem. 20 (2010) 2092–2098.
[23] X.L. Wu, Y.G. Guo, L.J. Wan, C.W. Hu, J. Phys. Chem. C 112 (2008) 16824–16829.
[24] Y. Jung, N. Singh, K.S. Choi, Angew. Chem. Int. Ed. Engl. 48 (2009) 1–5.
[25] J. Li, H.M. Dahn, L.J. Krause, D.B. Le, J.R. Dahn, J. Electrochem. Soc. 155 (2008) A812–A816.
[26] P.C. Wang, H.P. Ding, T. Bark, C.H. Chen, Electrochim. Acta 52 (2007) 6650–6655.
[27] Y. Yu, C.H. Chen, J.L. Shui, S. Xie, Angew. Chem. Int. Ed. Engl. 44 (2005) 7085–7089.
[28] Y.N. NuLi, P. Zhang, Z.P. Guo, P. Munroe, H.K. Liu, Electrochim. Acta 53 (2008) 4213–4218.